

Article

Impact of Hydrothermally Prepared Support on the Catalytic Properties of CuCe Oxide for Preferential CO Oxidation Reaction

Christos Papadopoulos ¹, Konstantinos Kappis ¹, Joan Papavasiliou ^{1,2,*}, John Vakros ³, Aspasia Antonelou ², Wojciech Gac ⁴, Haibin Li ⁵ and George Avgouropoulos ^{1,*}

¹ Department of Materials Science, University of Patras, GR-26504 Patras, Greece; c_papadopoulos@upatras.gr (C.P.); k.kappis@upatras.gr (K.K.)

² Foundation for Research and Technology-Hellas (FORTH), Institute of Chemical Engineering Sciences (ICE-HT), GR-26504 Patras, Greece; antonelou@iceht.forth.gr

³ Department of Chemistry, University of Patras, GR-26504 Patras, Greece; vakros@chemistry.upatras.gr

⁴ Faculty of Chemistry, Maria-Curie Skłodowska University, Pl. M. Curie-Skłodowskiej 3, 20-031 Lublin, Poland; wojtek.gac@poczta.umcs.lublin.pl

⁵ State Key Laboratory of Ocean Engineering, School of Naval Architecture, Ocean & Civil Engineering, Shanghai Jiao Tong University, Shanghai 200240, China; haibinli@sjtu.edu.cn

* Correspondence: ipapavas@upatras.gr (J.P.); geoavg@upatras.gr (G.A.)

Abstract: CuCe mixed oxide is one of the most studied catalytic systems for preferential CO oxidation (CO-PrOx) for the purification of hydrogen-rich gas stream. In this study, a series of ceria supports were prepared via a citrates-hydrothermal route by altering the synthesis parameters (concentration and temperature). The resulting supports were used for the preparation of CuCe mixed-oxide catalysts via wet impregnation. Various physicochemical techniques were utilized for the characterization of the resulting materials, whereas the CuCe oxide catalysts were assessed in CO-PrOx reaction. Through the proper modification of the hydrothermal parameters, CeO₂ supports with tunable properties can be formed, thus targeting the formation of highly active and selective catalysts. The nature of the reduced copper species and the optimum content in oxygen vacancies seems to be the key factors behind the remarkable catalytic performance of a CO-PrOx reaction.

Keywords: ceria; copper; catalyst; CO oxidation; PrOx; hydrogen; hydrothermal



Citation: Papadopoulos, C.; Kappis, K.; Papavasiliou, J.; Vakros, J.; Antonelou, A.; Gac, W.; Li, H.; Avgouropoulos, G. Impact of Hydrothermally Prepared Support on the Catalytic Properties of CuCe Oxide for Preferential CO Oxidation Reaction. *Catalysts* **2022**, *12*, 674. <https://doi.org/10.3390/catal12060674>

Academic Editor: Soghomon Boghosian

Received: 14 May 2022

Accepted: 16 June 2022

Published: 20 June 2022

Publisher's Note: MDPI stays neutral with regard to jurisdictional claims in published maps and institutional affiliations.



Copyright: © 2022 by the authors. Licensee MDPI, Basel, Switzerland. This article is an open access article distributed under the terms and conditions of the Creative Commons Attribution (CC BY) license (<https://creativecommons.org/licenses/by/4.0/>).

1. Introduction

In recent decades, carbon dioxide emissions have risen tremendously, leading to poor air quality and an increase in the global temperature by 1 °C [1]. Such a negative environmental impact originates from the massive utilization of fossil fuels in industry, electricity and transportation [2]. The Paris Agreement has set a goal to limit global warming to below 2 °C, preferably 1.5 °C, compared to pre-industrial levels [3]. Looking for a sustainable and decarbonized future for our planet, hydrogen may be an attractive solution, therefore many countries worldwide have already prepared their energy strategies and adapt hydrogen roadmaps towards 2050. Hydrogen is a non-toxic, environmentally friendly gas with a much higher heating value compared to that of gasoline or diesel [4,5]. Hydrogen fuel cell vehicles use hydrogen and oxygen to produce electricity [6], however, storing pure hydrogen in a mobile unit is a significant risk due to its low density and the high pressure that is required [7]. Thus, it is preferable to provide hydrogen to the fuel cell via a board or on-site reforming reaction of hydrogen carrier fuel. The starting fuel could be either liquid or gas, such as gasoline or methane, respectively, but alcohols such as methanol are more preferable because they can be considered as greener solutions [8,9]. After the steam reforming and the water gas shift reactions taking place, the final gas mixture consists of 45–75 vol.% H₂, 15–25 vol.% CO₂, 0.5–2 vol.% CO, N₂ and H₂O [10,11].

However, this small amount of CO can poison the Pt anode of the fuel cell, especially in the case of low temperature PEMFCs, so the special purification of the reformate gas mixture is required.

The cheapest and easiest way to remove CO from hydrogen-rich mixtures is via the preferential oxidation process (PrOx) [12,13]. The catalyst employed in the PrOx process should be active and highly selective towards CO oxidation at low temperatures (100–200 °C), minimizing the undesired loss of H₂ through oxidation. Various catalysts have been proposed in the literature. Noble metal-based catalysts (Pt, Pd, Rh, Ru) [14–18] have been reported from several groups, showing high activity and tolerance in the presence of excess CO₂ and H₂O; in the reformate gas stream, however, they cannot avoid hydrogen losses (low CO₂ selectivity). Gold-based catalysts [19–25] gained major attention after Haruta's work [17] who demonstrated the functionality of supported gold nanoparticles, smaller than 5 nm, achieving extraordinary activities for CO oxidation at low temperatures, even lower than ambient. However, these catalysts should operate at low temperatures to avoid H₂ oxidation, while they are sensitive in the presence of high concentrations of CO₂ and H₂O in the reaction mixture.

On the other hand, copper–cerium oxide catalysts represent an attractive non-precious metal-based catalytic system with comparable activity with noble metals, high stability, high tolerance in the presence of CO₂ and H₂O, and ideal selectivity at a temperature lower than 120 °C [26–36]. Thus, the scientific interest has focused on developing CuCe oxide catalysts, trying to tune the physicochemical characteristics responsible for their exceptional performance in the PrOx process. Copper oxide catalysts supported on cerium dioxide gather all the aforementioned advantages in addition to their low cost. Numerous studies have shown that the superiority of this system is based on the synergistic effect linked to strong copper–ceria interactions. Factors such as the redox interplay between Ce³⁺/Ce⁴⁺ and Cu²⁺/Cu⁺ redox couples, the presence of oxygen vacancies improving oxygen mobility, the superior reducibility of the mixed oxide and the nature of the active copper species (Cu⁺ and/or Cu²⁺) are crucial for the catalytic activity [26,27,37]. The morphology and the shape of the cerium oxide support plays a major part in these interactions. It is widely reported that the energy formation of oxygen vacancy defects depends on the exposed nanocrystal facets of ceria following the order {110} < {100} < {111} [38–40]. Zhou et al. [41] have shown that the concentration of oxygen vacancies is affected by the particle size proving that, in the case of 60 nm crystallites, the concentration of oxygen vacancies was two orders of magnitude lower than the 4 nm ones. The exposed crystal facets can also influence the nature of copper species formed on the ceria support. The dispersion of copper species is of prime importance for the activity and the selectivity of these catalysts in CO-PrOx process. Strongly interacting copper ions with ceria such as CuO clusters and surface Cu–O–Ce species have been proposed as the active phases [26–28,32,42]. Hydrothermal method is considered as one of the easiest ways to synthesize CeO₂ catalysts with different physicochemical characteristics by altering the experimental parameters such as temperature, reaction time and the concentration of the precipitating agent [43,44].

The aim of this work was to focus on the effect of ceria support on the activity and selectivity of CuCe oxide catalysts for the preferential oxidation of CO. In order to investigate this effect, different ceria samples were prepared using a citrates hydrothermal method [26,27]. A systematic study of the preparation parameters, such as the temperature of the hydrothermal route and concentration of precipitating agent, affecting the properties of ceria, was performed. The obtained ceria supports were used to disperse active copper species via wet impregnation, thus obtaining highly active CuCe oxide catalysts.

2. Results

2.1. Morphological Characteristics (SEM)

The samples prepared in this study are presented in Table 1. The samples are denoted as Ce-X-Y, or CuCe-X-Y for the ceria and the CuCe oxide catalysts, respectively, where X is the concentration of NaOH and T is the temperature applied in the hydrothermal method.

In this work, 3 hydrothermal temperatures (120 °C, 150 °C and 180 °C) and 3 concentrations of the precipitating agent NaOH (0.1 M, 1 M and 5 M), were employed.

Table 1. Specific surface area (SSA), mean pore diameter (MPD) and pore volume (PV) of ceria and CuCe oxides. The numbers in brackets refer to the CuCe oxide catalysts.

| Sample | C _{NaOH} -T (°C) | SSA (m ² g ⁻¹) | MPD (nm) | PV (cm ³ g ⁻¹) |
|----------------|---------------------------|---------------------------------------|-------------|---------------------------------------|
| (Cu)Ce-0.1-120 | 0.1M-120 | 29 (20) | 8.6 (8.3) | 0.038 (0.030) |
| (Cu)Ce-0.1-150 | 0.1M-150 | 30 (23) | 8.3 (9.0) | 0.038 (0.035) |
| (Cu)Ce-0.1-180 | 0.1M-180 | 25 (22) | 18.2 (14.6) | 0.087 (0.083) |
| (Cu)Ce-1-120 | 1M-120 | 74 (69) | 4.3 (4.3) | 0.16 (0.15) |
| (Cu)Ce-1-150 | 1M-150 | 75 (70) | 3.8 (3.6) | 0.14 (0.13) |
| (Cu)Ce-1-180 | 1M-180 | 69 (63) | 4.3 (4.0) | 0.15 (0.13) |
| (Cu)Ce-5-120 | 5M-120 | 128 (100) | 6.0 (6.1) | 0.21 (0.18) |
| (Cu)Ce-5-150 | 5M-150 | 42 (38) | 14.2 (16.4) | 0.19 (0.18) |
| (Cu)Ce-5-180 | 5M-180 | 38 (36) | 17.8 (16.6) | 0.22 (0.18) |

The variation of the preparation conditions provided nine ceria samples with different physicochemical properties. These samples were used for the dispersion of copper ions with wet impregnation method and loading at 7.5 wt.%. Figure 1 illustrates the morphologies of the nine hydrothermally prepared ceria materials with different experimental conditions. The concentration of NaOH was the main factor influencing the morphology of the samples. At low NaOH concentrations (0.1 M), the final solution before hydrothermal treatment was acidic with a pH = 2.52. When the solution was treated at low temperatures (120 °C and 150 °C), a rod-like morphology was dominant with a mean size of 2–10 µm. Further increase in the temperature synthesis (180 °C) resulted in the particles' agglomeration, with a non-well defined spherical morphology. In the case of higher NaOH concentrations (1 M and 5 M) the solution before the hydrothermal treatment was highly basic with a pH higher than 13. The hydrothermal temperature did not seem to influence the final morphology of the samples prepared with a moderate and high concentration of NaOH, since in all these cases, bulky aggregates with irregular size and geometry were formed. The particle formation process is governed by two different mechanisms, in agreement with previous reports [45–47]. On acidic solutions, Ostwald Ripening was the dominant particle formation mechanism [45–47]. Firstly, the crystals were formed and then smaller crystals were re-dissolved and re-deposited on the surfaces of larger particles, leading to rod-like or spherical morphologies [45,46]. On basic solutions, the oriented attachment mechanism took place [48] which involved the spontaneous self-organization of adjacent crystals influenced by the excess OH⁻ ions and the hydrothermal temperatures. This process led to the formation of bulky agglomerates. It should be noted that the impregnation of copper ions did not alter the morphology of pure ceria supports (Figure S1).

2.2. Textural Characteristics (N₂ Physisorption)

Figure 2 illustrates the pore volume distribution diagrams of the hydrothermally prepared pure ceria and the copper–cerium mixed oxide catalysts. Additionally, Table 1 presents the porosimetry characteristics of the samples such as the BET-specific surface area, the mean pore diameter and the total pore volume. Depending on the experimental parameters, the synthesized samples exhibited different specific surface areas and porosity. When low concentrations of NaOH (0.1 M) were applied, low SSA values were obtained at all temperatures (Table 1). The porosity remained the same at 120 °C and 150 °C with an extremely low total pore volume. At elevated temperatures (180 °C), small pores collapse and larger ones were formed due to particle agglomeration (Figure 2). As a result, lower values of SSA were measured for the samples prepared at 180 °C. Those findings are in line with the morphological characteristics discussed for SEM measurements (Figure 1).

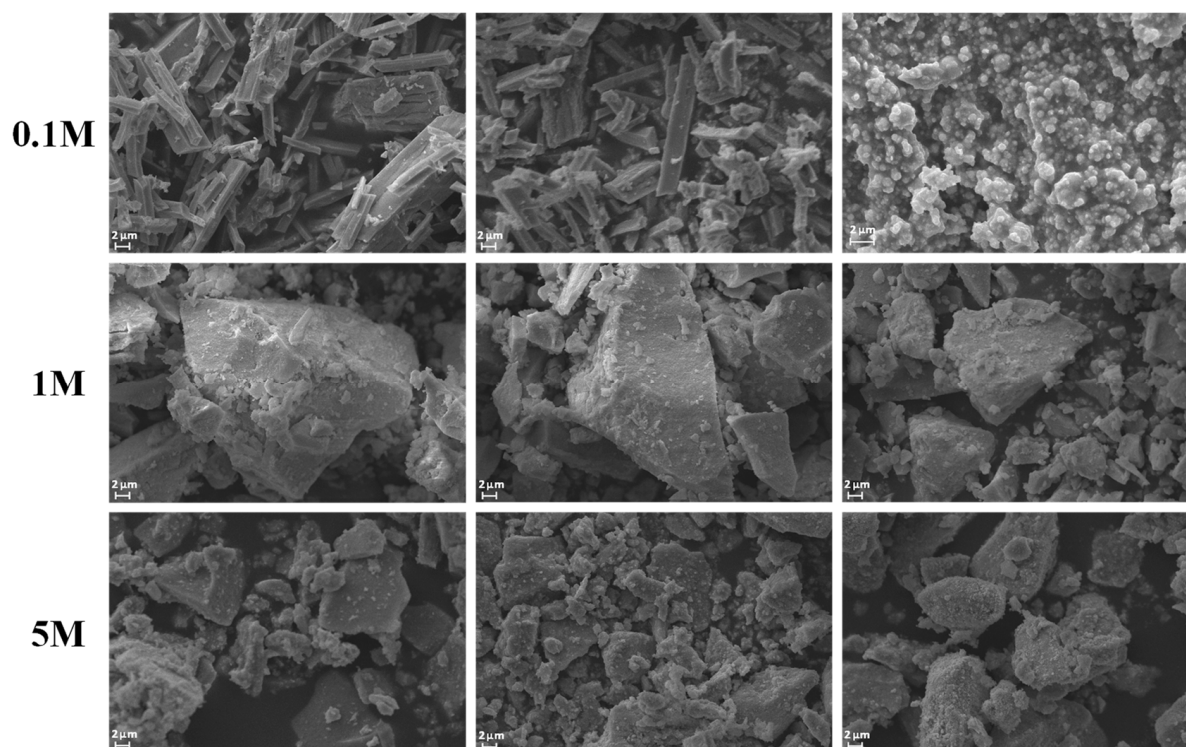


Figure 1. SEM images (scale bar at 2.0 μm) from the different hydrothermally prepared pure ceria substrates.

Higher NaOH concentrations influenced the porosity of the samples increasing the SSA. At medium concentrations (1 M), the hydrothermal temperature did not affect the textural characteristics. In every case a single peak distribution was present at the mesoporous range centered at approximately 6–7 nm (Figure 2) with SSA values between 69 and 75 $\text{m}^2 \text{g}^{-1}$. The highest SSA (128 $\text{m}^2 \text{g}^{-1}$) was achieved when the precursor was treated at 120 $^\circ\text{C}$ with 5 M of NaOH. This sample possessed a single peak distribution at the mesoporous range centered at approximately 9 nm. A further temperature increase (150 $^\circ\text{C}$ and 180 $^\circ\text{C}$) had a negative effect on the textural characteristics decreasing the SSA (Table 1). The pore distribution diagram was shifted to the macroporous range with a peak at approximately 30 nm, as previously discussed (Figure 2). As expected, the mixed oxide catalysts experienced a small decrease in their SSA due to the dispersion of copper ions onto the ceria surface. Moreover, the pore distribution was not affected and only a small reduction in the total pore volume can be observed in Figure 2, implying the good dispersion of copper ions on the support, as confirmed via SEM/EDS mapping (Figure S2).

2.3. Structural Characteristics (XRD)

Figure 3 depicts the XRD patterns of all prepared materials. In the case of pure ceria samples, it is evident that all peaks can be attributed to the (111), (200), (220), (331), (222), (400), (331), (420), and (422) crystal planes of face-centered cubic fluorite phase of CeO_2 [JCPDS: 00-043-1002] with an $Fm\bar{3}m$ space group and a lattice constant $a = 0.54113 \text{ nm}$ [49]. No other diffraction peaks were detected, suggesting the high purity of the prepared cerium oxides at any synthesis conditions employed. The peaks observed in Figure 3 are sharp, implying the high crystallinity of the prepared samples. Their intensity varies, where high intensity peaks imply particle agglomeration at high hydrothermal temperatures leading to the formation of bigger nanoparticles (see Table 2). The average crystallite size lay between 8.38 nm and 28.78 nm. The sample prepared at 120 $^\circ\text{C}$ with 5 M NaOH possessed the lowest average crystallite size which is in line with the specific surface areas results discussed above. Moreover, no peak shifts were observed, suggesting that there was no serious deformation of the crystal lattice neither solid solution formation. This is also

depicted in the slight changes of the value of the calculated lattice parameter a shown in Table 2. It is widely reported in the literature that higher crystal lattice values, a , in pure ceria can be attributed to the expansion of the crystal lattice due to the presence of Ce^{3+} ions which have a larger atomic radius than the Ce^{4+} [41,50,51]. It should be noted that, in this work, the lower temperature synthesized samples have higher values for a . Therefore, though it is weak evidence, the temperature can play a significant role in the tuning of surface vacancies. For nanocrystalline powders, the lattice parameter varied depending on the particle size which can be attributed to the grain surface relaxation [52]. Higher crystal lattice values, compared to that of bulk ceria, were reported for exceedingly small nanoparticles up to 4 nm [53,54]. On the other hand, the concentration of NaOH was also important for the presence of Ce^{3+} species. The hydroxy groups present at hydrothermal synthesis may stabilize small nanoparticles leading to smaller crystal lattice values [55]. It has been also reported that the powder's color change from white (bulk ceria) to yellow (CeO_{2-x}) might be an indication of the replacement of Ce^{4+} from Ce^{3+} ions [55]. In our case most of the samples have yellow powder color. Thus, we cannot draw a safe conclusion about the population of Ce^{3+} ions only from the crystal lattice parameters.

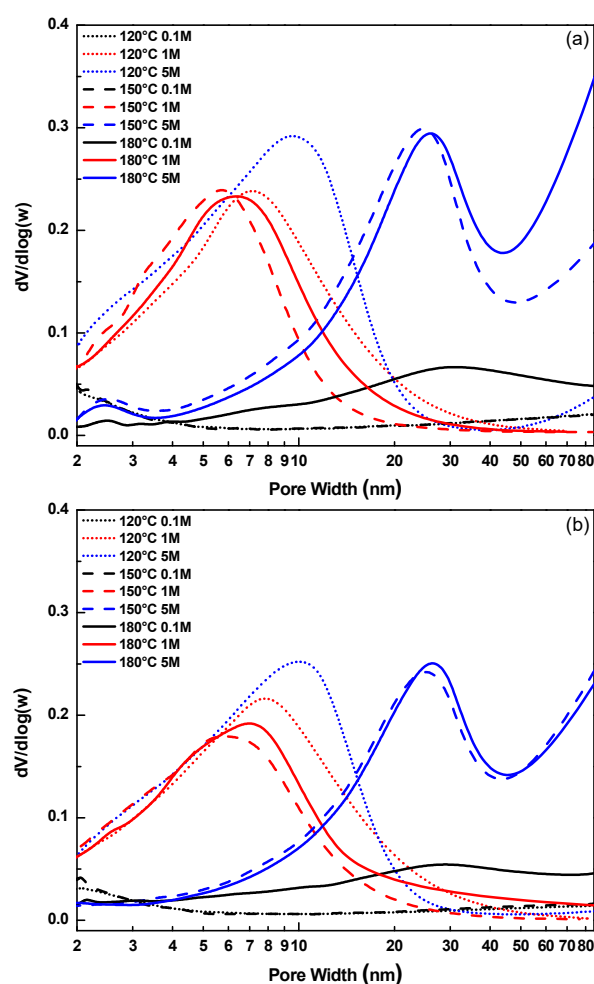


Figure 2. Pore size distribution of pure ceria supports (a) and CuCe oxide catalysts (b).

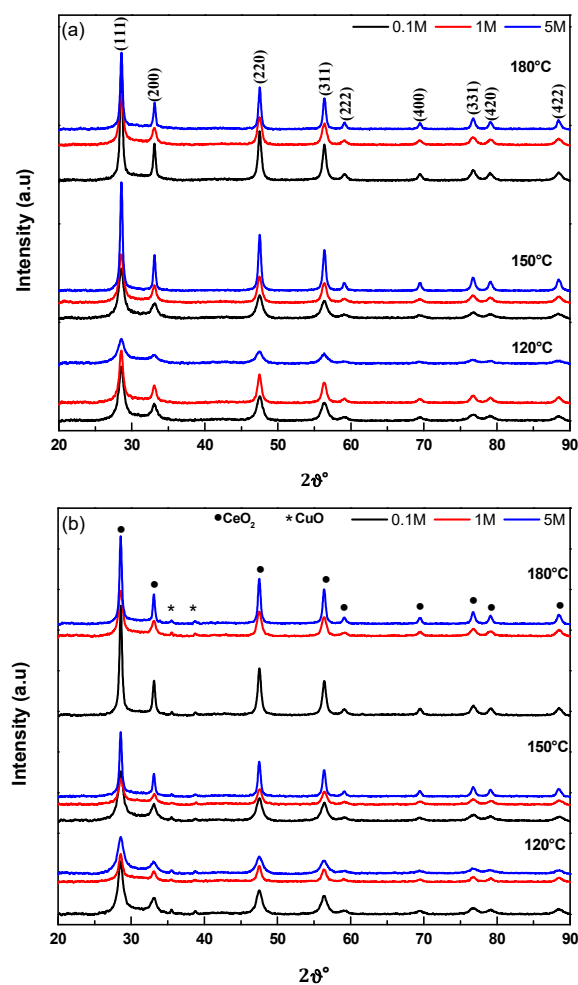


Figure 3. XRD patterns of hydrothermally prepared pure ceria (a) and CuCe oxide (b) samples.

Table 2. Average crystallite size (d_{111}) and lattice parameters (a) of pure ceria samples based on the crystal plane of (111) of CeO_2 .

| Sample | d_{111} (nm) ¹ | a (nm) ² |
|------------|-----------------------------|-----------------------|
| Ce-0.1-120 | 11.5 | 0.5406 |
| Ce-0.1-150 | 11.1 | 0.5404 |
| Ce-0.1-180 | 28.8 | 0.5408 |
| Ce-1-120 | 14.0 | 0.5412 |
| Ce-1-150 | 12.0 | 0.5410 |
| Ce-1-180 | 12.7 | 0.5410 |
| Ce-5-120 | 8.38 | 0.5410 |
| Ce-5-150 | 21.4 | 0.5407 |
| Ce-5-180 | 21.8 | 0.5407 |

¹ Calculated using Scherrer equation. ² Calculated from d_{111} spacing.

Concerning the CuCe oxide samples (Figure 2b), two extra peaks with very low intensity identified at 35.5° and 38.7° were attributed to the CuO crystal phase [JCPDS: 01-089-5896]. Excessively low intensity or/and broad peaks or even the absence of corresponding peaks suggest the good dispersion of Cu species onto the surface of ceria. The peaks assigned to CeO_2 did not shift while the crystal lattice parameters and the average crystal size of the CeO_2 remained more or less the same (values not shown), implying that copper ions were not incorporated into the crystal lattice. The average crystallite size of CuO could not be calculated via the Scherrer equation due to the hardly observed small

intensity of the corresponding peaks. Overall, it can be commented that crystalline CuO nanoparticles of small size were formed and dispersed on the ceria surface.

2.4. Redox Properties (H_2 -TPR)

The reducibility profiles of the CuCe oxide catalysts are illustrated at Figure 4. The TPR measurements may provide useful insight on the redox properties affected by different hydrothermal parameters, and as a consequence on the impact on the catalytic activity and selectivity. It was reported in the literature that the reduction in pure ceria exhibits two characteristic peaks, one that starts at temperatures higher than 300 °C with a maximum of approximately 500 °C, and one that starts at approximately 600 °C with a peak centered at 800 °C. The first peak is attributed to the reduction in surface oxygen species, whereas the second one is attributed to the reduction in bulk ceria oxygen and the Ce^{4+} into Ce^{3+} [56–58]. In this work, the latter peak was present in all samples. Pure CuO usually exhibits one major peak at ca. 300 °C with a shoulder at ca. 244 °C corresponding to the $CuO \rightarrow Cu_2O$ and $Cu_2O \rightarrow Cu$ transitions [59]. In our case, the complete reduction concerning copper species and the surface oxygen species of ceria, which lay within 195–225 °C, started at lower temperatures, even lower than 100 °C, depending on the sample. These temperatures are far lower compared to those of pure oxides. This superior reducibility of mixed oxides compared to the individual counterparts has been reviewed by Dong et al. [37] and attributed to the electronic metal–support interactions and the H_2 spillover from copper sites to the ceria support.

In this work, the synthesized mixed oxide materials exhibited four different reduction peaks correlated with the reduction in copper species with varying size and interaction with the support. These peaks are presented on the inset images of Figure 4 and summarized in Table 3 along with the corresponding peak temperatures. In the low temperature region, two reduction peaks are observed: peak (α') and peak (α). Peak α' is related with the reduction in ultrasmall CuO_x species, while peak α is attributed to the reduction in highly dispersed CuO_x clusters, strongly interacting with the ceria support [28,56,60–63]. Peak α' is only present at three samples (CuCe-1-120, CuCe-5-120 and CuCe-1-150) whereas peak α is present at every sample except CuCe-0.1-120. Concerning the high temperature reduction peaks, peak β is correlated with the reduction in the strongly bound surface Cu-[O_x]-Ce solid solution [64–66] and peak γ is attributed to the reduction in segregated larger copper entities weakly interacting with the ceria support [28,56,63]. Peak β is present in all sample profiles, whereas peak γ is present in the case of samples CuCe-0.1-120, CuCe-0.1-150, CuCe-0.1-180, CuCe-5-150 and CuCe-5-180. The total hydrogen consumption of these peaks is summarized in Table 3. It can be seen that although the samples were impregnated with the same amount of copper, the total hydrogen consumption slightly differs. As discussed earlier, the surface oxygen species of mixed copper ceria oxides were reduced at lower temperatures compared to pure ceria. Thus, the exhibited hydrogen consumption can be an indication of the population of the surface loosely bound oxygen of each ceria support. Low hydrothermal synthesis (120 °C) favored the formation of more surface oxygen species. The reduction peaks of these species coincide with peaks β and γ . As it will be discussed later, the nature of the copper species formed and the temperature where their reduction took place can play a crucial role on the catalytic activity.

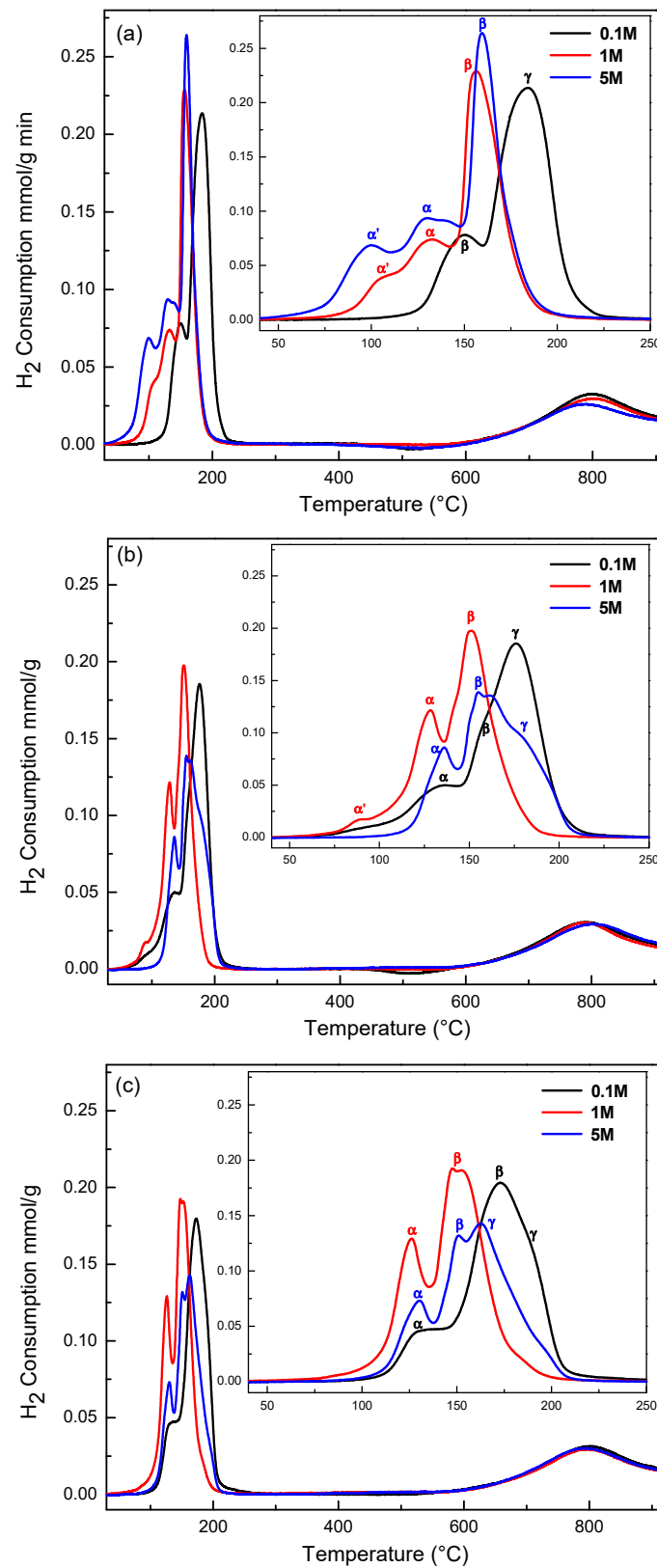


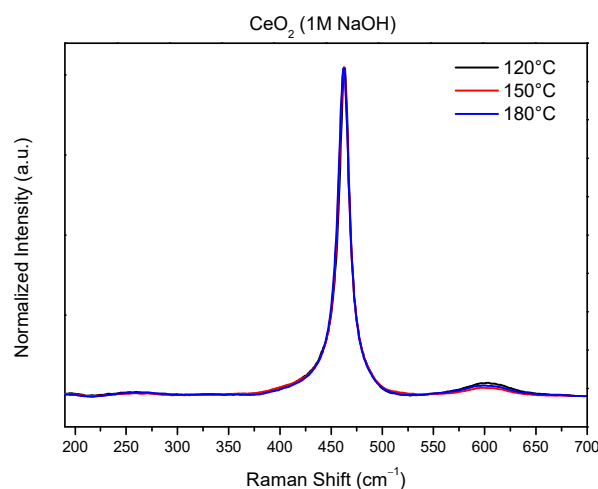
Figure 4. H₂-TPR profiles of the CuCe oxide catalysts obtained after hydrothermal treatment at 120 °C (a), 150 °C (b) and 180 °C (c). Magnification of the low temperature region is shown in the inset profiles.

Table 3. Redox properties of CuOCeO₂ catalysts.

| Sample | Peak α' (°C) | Peak α (°C) | Peak β (°C) | Peak γ (°C) | H ₂ Consumption ($\mu\text{mol H}_2 \text{ g}^{-1}$) |
|--------------|---------------------|--------------------|-------------------|--------------------|---|
| CuCe-0.1-120 | | | 150 | 184 | 918.7 |
| CuCe-0.1-150 | | 134 | 159 | 176 | 880.8 |
| CuCe-0.1-180 | | 130 | 173 | 188 | 842.1 |
| CuCe-1-120 | 105 | 132 | 157 | | 838.2 |
| CuCe-1-150 | 89 | 128 | 151 | | 851.6 |
| CuCe-1-180 | | 126 | 150 | | 838.5 |
| CuCe-5-120 | 99 | 130 | 160 | | 1073.0 |
| CuCe-5-150 | | 136 | 158 | 181 | 737.8 |
| CuCe-5-180 | | 131 | 151 | 163 | 724.7 |

2.5. Raman Analysis

In order to further examine the structural characteristics of CuCe catalysts, Raman spectroscopy measurements were performed. In Figure 5, the Raman spectra of the hydrothermally prepared pure ceria supports are illustrated for 1 M NaOH. All samples presented the characteristic F_{2g} vibration band at $\sim 464 \text{ cm}^{-1}$ of the fluorite phase of ceria. Additionally, the Raman band related to oxygen vacancies (D band) and the 2TA band were present at $\sim 595 \text{ cm}^{-1}$ and $\sim 265 \text{ cm}^{-1}$, respectively [67,68]. The linewidth of the F_{2g} vibration band was the same in all cases, showing that under a moderate concentration of NaOH, the variation of hydrothermal temperature did not influence the structure of the support. This feature is in line with the previous physicochemical measurements.

**Figure 5.** Raman spectra of pure ceria samples.

The addition of a copper oxide phase onto the hydrothermally prepared supports selected case of 1 M NaOH triggered a shift of the main peak towards lower wavenumbers and an increase in the content of lattice defects, as pointed out by the intensity ratio between the D and F_{2g} band ($I_D/I_{F_{2g}}$ ratio) (see Table 4). Therefore, it has been suggested that more oxygen vacancies were formed due to copper incorporation into the ceria phase [69,70]. Such a conclusion could not have been exclusively extracted from XRD measurements. However, it should be mentioned that the $I_D/I_{F_{2g}}$ ratio gives a rough estimation of oxygen vacancies, as CuO-related Raman band emerged in the same wavenumber range of the D band. In addition to the CeO₂-related Raman bands, Raman peaks related with the CuO phase were present. More specifically, the peaks at $\sim 292 \text{ cm}^{-1}$, $\sim 343 \text{ cm}^{-1}$, and 629 cm^{-1} were assigned to the Ag, B_{1g}, and B_{2g} modes, respectively [71]. Despite the fact that all the mixed oxides had the same copper loading, the intensity of CuO peaks was different depending on the employed ceria support (see Figure 6). For instance, for the CuCe-0.1

catalysts, the signal of the CuO peaks was almost absent. CuO attributed peaks were clearly evident in the CuCe-1M samples, and the same case was present in the CuCe-5M materials. These observations show that the surface of the resulting materials is quite inhomogeneous, a characteristic that is a common phenomenon when the impregnation method is applied [72].

2.6. Preferential Oxidation of CO in Excess H₂ (PrOx)

Figure 7 presents the catalytic activity tests, along with the selectivity of the CuCe materials, for the preferential oxidation reaction of CO. It is obvious that low concentrations of NaOH (0.1 M) led to poor catalytic activities. Between these three samples, higher hydrothermal treatment temperatures improved the catalytic activity. Samples prepared at medium concentrations (1 M NaOH) experienced the best catalytic results. Higher hydrothermal temperatures (150 °C and 180 °C) favored the catalytic activity of these samples. The catalyst with a ceria support hydrothermally prepared at 1 M NaOH and 150 °C exhibited the best catalytic performance with a complete CO conversion at 130 °C combined with a selectivity of 90.2% towards CO₂. High NaOH concentrations (5 M) led to lower catalytic activities compared to 1 M concentrations. In this case, high hydrothermal temperatures had a negative influence on the catalytic activity, in contrast with the other two NaOH concentrations (0.1 M and 1 M).

Table 4. Peak position of the F_{2g} vibration band and the relative amount of oxygen vacancies (I_D/I_{F2g}) of CuO/CeO₂ catalysts.

| Samples | F _{2g} Peak Position (cm ⁻¹) | I _D /I _{F2g} |
|--------------------------------------|---|----------------------------------|
| CeO₂ supports | | |
| Ce-1M-120 | 463.4 | 0.039 |
| Ce-1M-150 | 462.6 | 0.023 |
| Ce-1M-180 | 462.6 | 0.029 |
| CuO/CeO₂ catalysts | | |
| CuCe-0.1-120 | 460.7 | 0.036 |
| CuCe-0.1-150 | 460.7 | 0.041 |
| CuCe-0.1-180 | 459.6 | 0.034 |
| CuCe-1-120 | 460.9 | 0.107 |
| CuCe-1-150 | 462.1 | 0.070 |
| CuCe-1-180 | 459.6 | 0.080 |
| CuCe-5-120 | 454.5 | 0.243 |
| CuCe-5-150 | 457.0 | 0.067 |
| CuCe-5-180 | 452.6 | 0.087 |

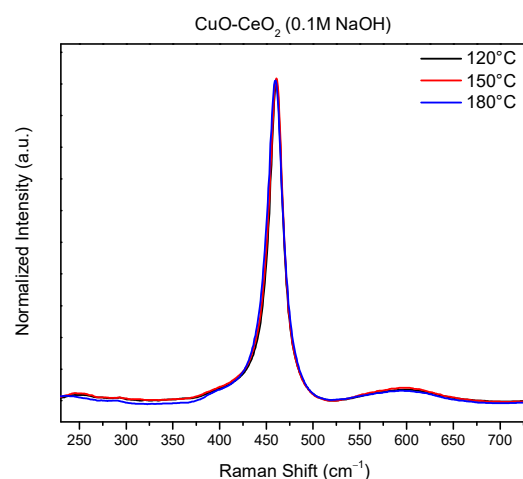


Figure 6. Cont.

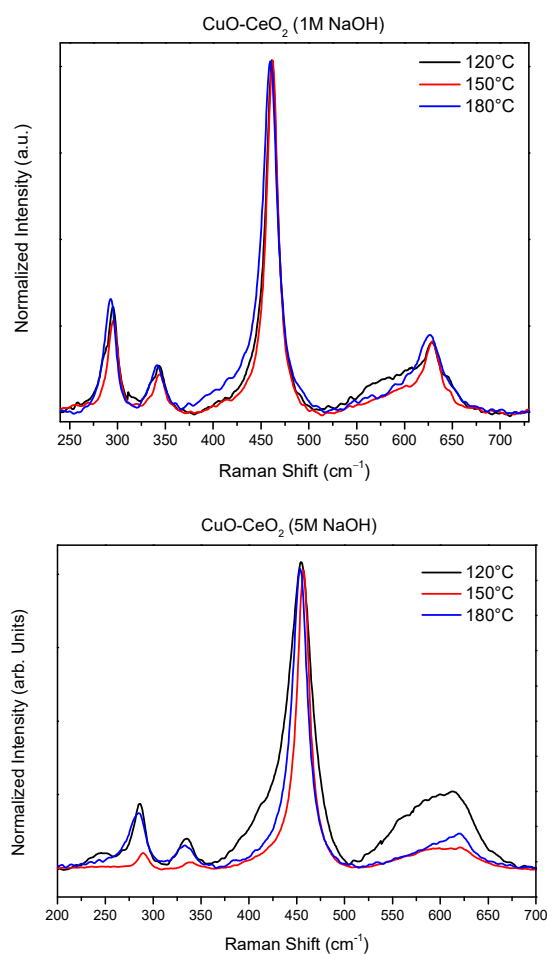


Figure 6. Raman spectra of the CuO-CeO₂ samples.

The values for T_{50} and T_{95} , i.e., the temperatures where the 50% and 95% conversion of CO was achieved, respectively, are summarized at the bar graph of Figure 8. It can be commented that the combination of the hydrothermal temperature and the concentration of the precipitating agent (NaOH) employed in the synthesis of the ceria support significantly influenced the PrOx performance of the mixed oxide catalysts.

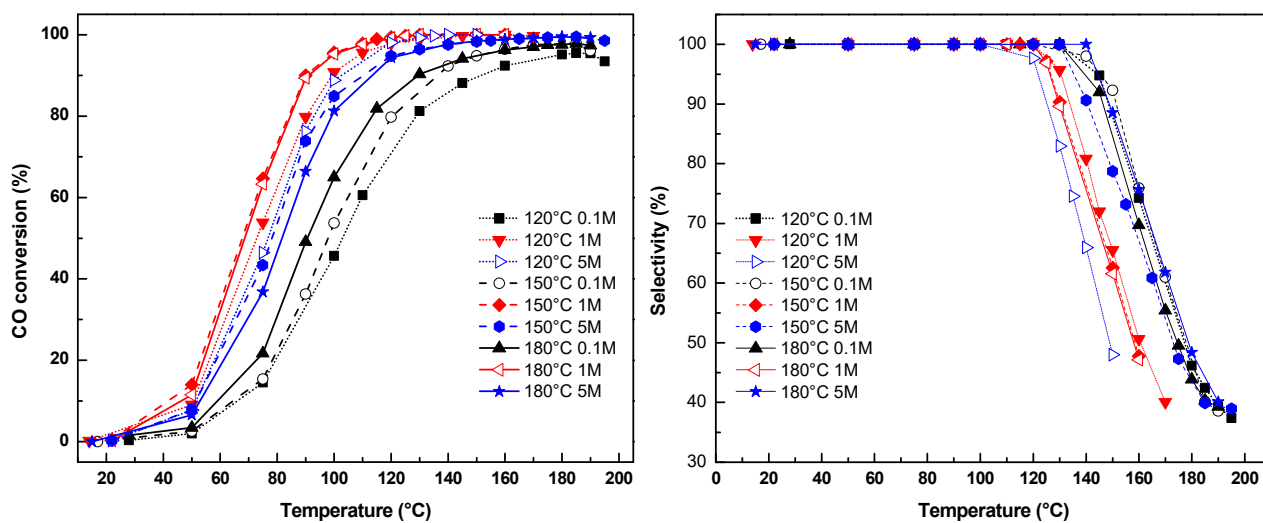


Figure 7. CO conversion and selectivity curves for the CuCe oxide catalysts.

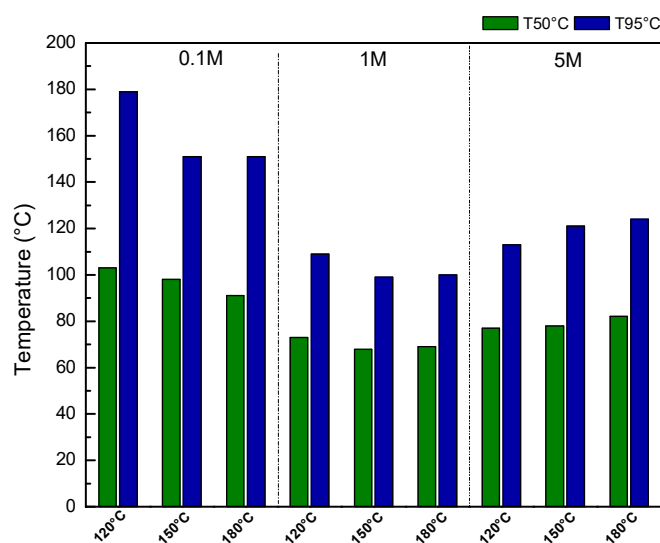


Figure 8. Temperatures of 50% (T_{50}) and 95% (T_{95}) of CO conversion for the CuCe oxide catalysts.

2.7. Correlation of Physicochemical Properties with Catalytic Performance

The achievement of high activity and selectivity for CO-PrOx reaction over CuCe oxide catalysts is closely related with the reduced copper species and the optimum concentration of oxygen vacancies. H_2 -TPR measurements suggested that the role of the highly dispersed CuO_x clusters, and the strongly bound surface solid solution of Cu-[O_x]-Ce (peak α and β , respectively), along with the surface oxygen species of ceria, is crucial for catalytic activity. These species play a dominant role in the Mars–van Krevelen redox type mechanism proposed in the literature [28,73–75], which facilitates the formation of active Cu^+ ions through the redox equilibrium $Ce^{4+} + Cu^+ \leftrightarrow Ce^{3+} + Cu^{2+}$. Furthermore, according to previous studies [58,66], the existence of Cu-[O_x]-Ce species promotes the catalytic performance of CuCe catalysts. For example, Du et al. [66] found that strongly bound Cu-[O_x]-Ce species can act as a reservoir for Cu^+ species during CO-PrOx reaction. Additionally, Guo and Zhou [58] found that Cu-[O_x]-Ce species promote the catalytic behavior of catalysts through the enhanced copper–ceria interaction. On the other hand, catalysts containing larger copper entities weakly interacting with ceria support (peak γ) exhibit poor catalytic activity. This is due to their larger size, responsible for their poor reducibility on relative reaction temperatures. Moreover, these entities affect CO_2 selectivity [76]. Considering the aforementioned findings, it can be commented that a capable concentration of CuO_x and Cu-[O_x]-Ce species that are reduced at low temperatures (see Table 3) is crucial for high activity and selectivity. The Raman spectroscopy measurements indicated that an optimum concentration of oxygen vacancies is also required in order to obtain high catalytic activity. The CuCe-1M series and especially the CuCe-1M-150 sample, despite presenting a moderate concentration of oxygen vacancies (see Table 4), outperformed the catalyst with the highest concentration of oxygen vacancies (CuCe-5M-120). These results are in agreement with previous studies [27,77] which concluded that a highly defective structure does not guarantee high catalytic activity.

3. Materials and Methods

3.1. Catalysts Preparation

Various pure ceria materials were synthesized via a hydrothermal method where citric acid ($C_6H_8O_7$) was employed as the chelating agent. The role of citric acid was discussed in detail in our previous work [27]. Moreover, cerium nitrate ($Ce(NO_3)_3 \cdot 6H_2O$) was chosen as the ceria precursor and sodium hydroxide solution (NaOH), in three different concentrations (0.1 M, 1 M and 5 M), as the precipitating agent. All the reagents used were of analytical grade. Firstly, the reagents were diluted in specific amounts of triply distilled water and then mixed in a total volume of 180 cm^3 . The solution remained under stirring

for 30 min. The molar ratio of citric acid/Ce was equal to 1. Then, the solution was transferred in a Teflon beaker of 230 cm³ and hydrothermally treated in a stainless-steel autoclave (chamber volume of ca. 250 cm³) for 24 h at three different temperatures (120 °C, 150 °C and 180 °C). After the hydrothermal treatment, the formed pastes were filtrated and washed with several amounts of warm triply distilled water to remove excess Na⁺. Finally, the samples were dried at 75 °C for 12 h and calcined in static air at 400 °C for 2 h with a heating ramp of 2 °C min⁻¹. Nine different oxides were synthesized following the example encoding of CeO₂ 0.1 M 120 °C, where 0.1 M indicates the concentration of NaOH employed and 120 °C the hydrothermal treatment temperature.

The CuCe mixed oxide catalysts were prepared via the wet impregnation method using a rotary evaporator. Copper nitrate (Cu(NO₃)₂·2.5H₂O) was dissolved in 25 cm³ of triply distilled water and mixed with an appropriate amount of the previously hydrothermally prepared ceria. All catalysts were loaded with 7.5 wt.%. After mixing, the solution remained under mild stirring for 1 h. Subsequently, excess water was removed under vacuum using the rotary evaporator (45 °C water bath and 60 rpm). Finally, the obtained paste was collected, dried for 12 h at 75 °C and calcined in static air for 2 h. Similar encoding was followed as above.

3.2. Catalysts Characterization

The morphology of the samples was investigated via an Zeiss EVO MA 10 scanning electron microscope (SEM).

Textural characteristics were determined by N₂ physisorption at −196 °C using a NOVAtouch LX gas sorption system. The specific surface area was calculated via the Brunauer–Emmett–Teller (BET) equation and the pore size distribution was determined by the BJH method. Prior to analysis, the samples were outgassed for 1 h at 120 °C under vacuum.

The crystallite structure was determined using an X-ray powder diffractometer (Bruker D8 Advance, Bruker, Birmingham, UK) using CuK_α radiation ($\lambda = 0.15418$ nm) at 40 kV and 40 mA.

Temperature-programmed reduction studies of the CuCe oxide catalysts were carried out using an Autochem II 2920 (Micromeritics Instrument Corp., Norcross, GA, USA), equipped with a TCD detector. The catalysts were initially heated up to 300 °C in a gas flow of 5% O₂/He mixture. After cooling down to room temperature, they were treated in the flow of a gas mixture consisting of 5% H₂ in Ar. The total gas flow rate was 30 cm³ min⁻¹ with a temperature increase rate of 10 °C min⁻¹. The formed water was removed in a cold trap maintained in liquid nitrogen (LN₂)–isopropyl alcohol mixture at ca. −90 °C.

Raman spectra were accumulated with the 441.6 nm laser line as the excitation source emerging from a He–Cd laser (Kimon). The scattered light was analyzed by the Lab-Ram HR800 (Jobin-Yvon, Edison, NJ, USA) micro-Raman spectrometer at a spectral resolution of approximately 2.0 cm⁻¹. A microscope objective with magnification 50x was used to focus the light onto a spot of ~3 μm in diameter. Low laser intensities were used (~0.37 mW on the sample) to avoid spectral changes due to heat-induced effects. The Raman shift was calibrated using the 520 cm⁻¹ Raman band of crystalline Si.

3.3. Catalytic Activity Tests

The catalysts were evaluated in the preferential oxidation of CO in excess H₂. The activity and selectivity tests were conducted at atmospheric pressure, in the temperature range of 20–200 °C, in a conventional fixed-bed reactor system described elsewhere [78]. 120 mg of catalyst in powder form were placed in a quartz reactor with a quartz wool catalytic bed. The feed stream consisted of 1 vol.% CO, 1.25 vol.% O₂, 50 vol.% H₂ and He as carrier gas with a total flow rate of 50 cm³/min, yielding a contact time of W/F = 0.144 g s cm⁻³. The product and reactant analysis were carried out by a gas chromatograph (Shimadzu GC-14A) equipped with a TCD detector. The CO conversion

calculation was based on the CO consumption or CO₂ formation. The selectivity towards CO₂ production was calculated from the oxygen mass balance.

4. Conclusions

In this study, the effect of ceria on the performance of CuCe oxide catalysts for CO-PrOx reaction was examined. Various pure ceria supports were prepared by tuning the hydrothermal parameters (concentration of NaOH and temperature of hydrothermal treatment) while the wet-impregnation method was utilized for the dispersion of copper oxide species on the ceria surface. The physicochemical characterization indicated that the appropriate combination of hydrothermal parameters can provide ceria supports with desirable properties and subsequently result in the formation of highly active CuCe oxide catalysts. The CuCe-1M series and especially the CuCe-1M-150 sample exhibited a high catalytic activity and selectivity for CO-PrOx reaction, achieving complete CO conversion at 130 °C accompanied with a selectivity of 90.2% towards CO₂. Overall, it can be suggested that the nature of reduced copper species and the optimum content in oxygen vacancies play a critical role in achieving high catalytic performance.

Supplementary Materials: The following supporting information can be downloaded at: <https://www.mdpi.com/article/10.3390/catal12060674/s1>. Figure S1: Representative SEM images of the CuCe oxide catalysts. The scale bar is adjusted to 2.0 μm; Figure S2: SEM/EDX images of the CuCe oxide catalysts. Scale bar is adjusted to 10 μm. The white dots illustrate the dispersion of Cu species onto the ceria support.

Author Contributions: Conceptualization and methodology, G.A., J.P. and J.V.; investigation, validation and formal analysis, C.P., K.K., A.A., W.G. and H.L.; writing—review and editing and supervision, J.P. and G.A. All authors have read and agreed to the published version of the manuscript.

Funding: This research was funded by the Research Committee of the University of Patras in Greece, via “K. Karatheodori” program, grant number (E.610). Co-financed by Inter-Governmental Cooperative Key Special Project under National Key R&D Program of China, grant number 2017YFE0184100.

Data Availability Statement: Not applicable.

Acknowledgments: Thanks are due to V. Karoutsos for his help in SEM measurements.

Conflicts of Interest: The authors declare no conflict of interest.

References

1. Opoku, E.E.O.; Dogah, K.E.; Aluko, O.A. The contribution of human development towards environmental sustainability. *Energy Econ.* **2022**, *106*, 105782. [CrossRef]
2. Li, L.; Khodakarami, S.; Yan, X.; Fazle Rabbi, K.; Gunay, A.A.; Stillwell, A.; Miljkovic, N. Enabling Renewable Energy Technologies in Harsh Climates with Ultra-Efficient Electro-Thermal Desnowing, Defrosting, and Deicing. *Adv. Funct. Mater.* **2022**. [CrossRef]
3. Rogelj, J.; Luderer, G.; Pietzcker, R.C.; Kriegler, E.; Schaeffer, M.; Krey, V.; Riahi, K. Energy system transformations for limiting end-of-century warming to below 1.5 C. *Nat. Clim. Change* **2015**, *6*, 519–527. [CrossRef]
4. Abe, J.O.; Popoola, A.P.I.; Ajenifuja, E.; Popoola, O.M. Hydrogen energy, economy and storage: Review and recommendation. *Int. J. Hydrogen Energy* **2019**, *44*, 15072–15086. [CrossRef]
5. Staffell, I.; Scamman, D.; Abad, A.V.; Balcombe, P.; Dodds, P.E.; Ekins, P.; Ward, K.R. The role of hydrogen and fuel cells in the global energy system. *Energy Environ. Sci.* **2019**, *12*, 463–491. [CrossRef]
6. Manoharan, Y.; Hosseini, S.E.; Butler, B.; Alzahrani, H.; Senior, B.T.F.; Ashuri, T.; Krohn, J. Hydrogen fuel cell vehicles; current status and future prospect. *Appl. Sci.* **2019**, *9*, 2296. [CrossRef]
7. Eftekhari, A.; Fang, B. Electrochemical hydrogen storage: Opportunities for fuel storage, batteries, fuel cells, and supercapacitors. *Int. J. Hydrogen Energy* **2017**, *42*, 25143–25165. [CrossRef]
8. Ghenciu, A.F. Review of fuel processing catalysts for hydrogen production in PEM fuel cell systems. *Curr. Opin. Solid State Mater. Sci.* **2002**, *6*, 389–399. [CrossRef]
9. Papavasiliou, J.; Avgouropoulos, G.; Ioannides, T. In situ combustion synthesis of structured Cu-Ce-O and Cu-Mn-O catalysts for the production and purification of hydrogen. *Appl. Catal. B Environ.* **2006**, *66*, 168–174. [CrossRef]
10. Lindström, B.; Pettersson, L.J. Hydrogen generation by steam reforming of methanol over copper-based catalysts for fuel cell applications. *Int. J. Hydrogen Energy* **2001**, *26*, 923–933. [CrossRef]

11. Peppley, B.A.; Amphlett, J.C.; Kearns, L.M.; Mann, R.F.; Roberge, P.R. Hydrogen generation for fuel-cell power systems by high-pressure catalytic methanol-steam reforming. In Proceedings of the Thirty-Second Intersociety Energy Conversion Engineering Conference, Honolulu, HI, USA, 27 July–1 August 1997.
12. Joensen, F.; Rostrup-Nielsen, J.R. Conversion of hydrocarbons and alcohols for fuel cells. *J. Power Sources* **2002**, *105*, 195–201. [[CrossRef](#)]
13. Laguna, O.H.; Sarria, F.R.; Centeno, M.A.; Odriozola, J.A. Gold supported on metal-doped ceria catalysts (M=Zr, Zn and Fe) for the preferential oxidation of CO (PROX). *J. Catal.* **2010**, *276*, 360–370. [[CrossRef](#)]
14. Hashmi, A.S.K.; Hutchings, G.J. Gold catalysis. *Angew. Chem. Int. Ed.* **2006**, *45*, 7896–7936. [[CrossRef](#)] [[PubMed](#)]
15. Son, I.H.; Shamsuzzoha, M.; Lane, A.M. Promotion of Pt/ γ -Al₂O₃ by new pretreatment for low-temperature preferential oxidation of CO in H₂ for PEM fuel cells. *J. Catal.* **2002**, *210*, 460–465. [[CrossRef](#)]
16. Koo, K.Y.; Jung, U.H.; Yoon, W.L. A highly dispersed Pt/ γ -Al₂O₃ catalyst prepared via deposition–precipitation method for preferential CO oxidation. *Int. J. Hydrogen Energy* **2014**, *39*, 5696–5703. [[CrossRef](#)]
17. Haruta, M.; Kobayashi, T.; Sano, H.; Yamada, N. Novel gold catalysts for the oxidation of carbon monoxide at a temperature far below 0 °C. *Chem. Lett.* **1987**, *16*, 405–408. [[CrossRef](#)]
18. Igarashi, H.; Uchida, H.; Suzuki, M.; Sasaki, Y.; Watanabe, M. Removal of carbon monoxide from hydrogen-rich fuels by selective oxidation over platinum catalyst supported on zeolite. *Appl. Catal. A Gen.* **1997**, *159*, 159–169. [[CrossRef](#)]
19. Avgouropoulos, G.; Manzoli, M.; Boccuzzi, F.; Tabakova, T.; Papavasiliou, J.; Ioannides, T.; Idakiev, V. Catalytic performance and characterization of Au/doped-ceria catalysts for the preferential CO oxidation reaction. *J. Catal.* **2008**, *256*, 237–247. [[CrossRef](#)]
20. Manzoli, M.; Avgouropoulos, G.; Tabakova, T.; Papavasiliou, J.; Ioannides, T.; Boccuzzi, F. Preferential CO oxidation in H₂-rich gas mixtures over Au/doped ceria catalysts. *Catal. Today* **2008**, *138*, 239–243. [[CrossRef](#)]
21. Tabakova, T.; Avgouropoulos, G.; Papavasiliou, J.; Manzoli, M.; Boccuzzi, F.; Tenchev, K.; Ioannides, T. CO-free hydrogen production over Au/CeO₂–Fe₂O₃ catalysts: Part 1. Impact of the support composition on the performance for the preferential CO oxidation reaction. *Appl. Catal. B Environ.* **2011**, *101*, 256–265. [[CrossRef](#)]
22. Laguna Espitia, O.H.; Centeno Gallego, M.Á.; Arzamendi, G.; Gandía, L.M.; Romero Sarria, F.; Odriozola Gordón, J.A. (2010). Iron-modified ceria and Au/Ceria catalysts for total and preferential oxidation of CO (TOX and PROX). *Catal. Today* **2010**, *157*, 155–159. [[CrossRef](#)]
23. Scirè, S.; Crisafulli, C.; Riccobene, P.M.; Patanè, G.; Pistone, A. Selective oxidation of CO in H₂-rich stream over Au/CeO₂ and Cu/CeO₂ catalysts: An insight on the effect of preparation method and catalyst pretreatment. *Appl. Catal. A Gen.* **2012**, *417*, 66–75. [[CrossRef](#)]
24. Fu, Q.; Weber, A.; Flytzani-Stephanopoulos, M. Nanostructured Au–CeO₂ catalysts for low-temperature water–gas shift. *Catal. Lett.* **2001**, *77*, 87–95. [[CrossRef](#)]
25. Qiu, Z.; Guo, X.; Mao, J.; Zhou, R. The catalytic performance of isolated-dispersed Au on nanosized CeO₂ for CO preferential oxidation in H₂-rich stream. *Appl. Surf. Sci.* **2019**, *481*, 1072–1079. [[CrossRef](#)]
26. Papadopoulos, C.; Kappis, K.; Papavasiliou, J.; Vakros, J.; Kuśmierz, M.; Gac, W.; Avgouropoulos, G. Copper-promoted ceria catalysts for CO oxidation reaction. *Catal. Today* **2020**, *355*, 647–653. [[CrossRef](#)]
27. Kappis, K.; Papadopoulos, C.; Papavasiliou, J.; Vakros, J.; Georgiou, Y.; Deligiannakis, Y.; Avgouropoulos, G. Tuning the catalytic properties of copper-promoted nanoceria via a hydrothermal method. *Catalysts* **2019**, *9*, 138. [[CrossRef](#)]
28. Lykaki, M.; Pachatouridou, E.; Carabineiro, S.A.; Iliopoulou, E.; Andriopoulou, C.; Kallithrakas-Kontos, N.; Konsolakis, M. Ceria nanoparticles shape effects on the structural defects and surface chemistry: Implications in CO oxidation by Cu/CeO₂ catalysts. *Appl. Catal. B Environ.* **2018**, *230*, 18–28. [[CrossRef](#)]
29. Wang, B.; Zhang, H.; Xu, W.; Li, X.; Wang, W.; Zhang, L.; Liu, Z. Nature of active sites on Cu–CeO₂ catalysts activated by high-temperature thermal aging. *ACS Catal.* **2020**, *10*, 12385–12392. [[CrossRef](#)]
30. Guo, X.; Qiu, Z.; Mao, J.; Zhou, R. Shape-controlled Cu_xCe_{1-x}O₂ nanorods catalyst and the active components functioned in selective oxidation of CO in hydrogen-rich stream. *J. Power Sources* **2020**, *451*, 227757. [[CrossRef](#)]
31. Cruz, A.R.M.; Assaf, E.M.; Gomes, J.F.; Assaf, J.M. Active copper species of co-precipitated copper-ceria catalysts in the CO-PROX reaction: An in situ XANES and DRIFTS study. *Catal. Today* **2021**, *381*, 42–49. [[CrossRef](#)]
32. Martínez-Arias, A.; Gamarra, D.; Hungría, A.B.; Fernández-García, M.; Munuera, G.; Hornés, A.; Bera, P.; Conesa, J.C.; Cámara, A.L. Characterization of Active Sites/Entities and Redox/Catalytic Correlations in Copper-Ceria-Based Catalysts for Preferential Oxidation of CO in H₂-Rich Streams. *Catalysts* **2013**, *3*, 378–400. [[CrossRef](#)]
33. Gong, X.; Liu, B.; Kang, B.; Xu, G.; Wang, Q.; Jia, C.; Zhang, J. Boosting Cu-Ce interaction in Cu_xO/CeO₂ nanocube catalysts forenhanced catalytic performance of preferential oxidation of CO in H₂-rich gases. *Mol. Catal.* **2017**, *436*, 90–99. [[CrossRef](#)]
34. Wang, J.; Zhong, L.; Lu, J.; Chen, R.; Lei, Y.; Chen, K.; Han, C.; He, S.; Wan, G.; Luo, Y. A solvent-free method to rapidly synthesize CuO–CeO₂ catalysts to enhance their CO preferential oxidation: Effects of Cu loading and calcination temperature. *Mol. Catal.* **2017**, *443*, 241–252. [[CrossRef](#)]
35. Zou, Q.; Zhao, Y.; Jin, X.; Fang, J.; Li, D.; Li, K.; Lu, J.; Luo, Y. Ceria-nano supported copper oxide catalysts for CO preferential oxidation: Importance of oxygen species and metal-support interaction. *Appl. Surf. Sci.* **2019**, *494*, 1166–1176. [[CrossRef](#)]
36. Papavasiliou, J. Interaction of atomically dispersed gold with hydrothermally prepared copper-cerium oxide for preferential CO oxidation reaction. *Catal. Today* **2020**, *357*, 684–693. [[CrossRef](#)]

37. Dong, L.; Yao, X.; Chen, Y. Interactions among supported copper-based catalyst components and their effects on performance: A review. *Chin. J. Catal.* **2013**, *34*, 851–864. [[CrossRef](#)]
38. Paier, J.; Penschke, C.; Sauer, J. Oxygen Defects and Surface Chemistry of Ceria: Quantum Chemical Studies Compared to Experiment. *Chem. Rev.* **2013**, *113*, 3949–3985. [[CrossRef](#)]
39. Skorodumova, N.V.; Baudin, M.; Hermansson, K. Surface properties of CeO₂ from first principles. *Phys. Rev. B* **2004**, *69*, 075401. [[CrossRef](#)]
40. Baudin, M.; Wójcik, M.; Hermansson, K. Dynamics, structure and energetics of the (111), (011) and (001) surfaces of ceria. *Surf. Sci.* **2000**, *468*, 51–61. [[CrossRef](#)]
41. Zhou, X.-D.; Huebner, W. Size-induced lattice relaxation in CeO₂ nanoparticles. *Appl. Phys. Lett.* **2001**, *79*, 3512–3514. [[CrossRef](#)]
42. Avgouropoulos, G.; Ioannides, T. Selective CO oxidation over CuO–CeO₂ catalysts prepared via the urea–nitrate combustion method. *Appl. Catal. A* **2003**, *244*, 155–167. [[CrossRef](#)]
43. Terribile, D.; Trovarelli, A.; Llorca, J.; de Leitenburg, C.; Dolcetti, G. The Synthesis and Characterization of Mesoporous High-Surface Area Ceria Prepared Using a Hybrid Organic/Inorganic Route. *J. Catal.* **1998**, *178*, 299–308. [[CrossRef](#)]
44. Shan, W.; Guo, H.; Liu, C.; Wang, X. Controllable preparation of CeO₂ nanostructure materials and their catalytic activity. *J. Rare Earths* **2012**, *30*, 665–669. [[CrossRef](#)]
45. Wu, N.-C.; Shi, E.-W.; Zheng, Y.-Q.; Li, W.-J. Effect of pH of Medium on Hydrothermal Synthesis of Nanocrystalline Cerium(IV) Oxide Powders. *J. Am. Ceram. Soc.* **2002**, *85*, 2462–2468. [[CrossRef](#)]
46. Lin, M.; Fu, Z.Y.; Tan, H.R.; Tan, J.P.Y.; Ng, S.C.; Teo, E. Hydrothermal Synthesis of CeO₂ Nanocrystals: Ostwald Ripening or Oriented Attachment? *Cryst. Growth Des.* **2012**, *12*, 3296–3303. [[CrossRef](#)]
47. Alemán, J.; Chadwick, A.V.; He, J.; Hess, M.; Horie, K.; Jones, R.G.; Kratochvíl, P.; Meisel, I.; Mita, I.; Moad, G.; et al. Definitions of terms relating to the structure and processing of sols, gels, networks, and inorganic-organic hybrid materials (IUPAC Recommendations 2007). *Pure Appl. Chem.* **2007**, *79*, 1801–1827. [[CrossRef](#)]
48. Pan, C.; Zhang, D.; Shi, L. CTAB assisted hydrothermal synthesis, controlled conversion and CO oxidation properties of CeO₂ nanoplates, nanotubes, and nanorods. *J. Solid State Chem.* **2008**, *181*, 1298–1306. [[CrossRef](#)]
49. Montini, T.; Melchionna, M.; Monai, M.; Fornasiero, P. Fundamentals and Catalytic Applications of CeO₂-Based Materials. *Chem. Rev.* **2016**, *116*, 5987–6041. [[CrossRef](#)]
50. Zhang, W.; Niu, X.; Chen, L.; Yuan, F.; Zhu, Y. Soot Combustion over Nanostructured Ceria with Different Morphologies. *Sci. Rep.* **2016**, *6*, 29062. [[CrossRef](#)]
51. Xu, B.; Zhang, Q.; Yuan, S.; Zhang, M.; Ohno, T. Morphology control and characterization of broom-like porous CeO₂. *Chem. Eng. J.* **2015**, *260*, 126–132. [[CrossRef](#)]
52. Maensiri, S.; Masingboon, C.; Laokul, P.; Jareonboon, W.; Promarak, V.; Anderson, A.P.L.; Seraphin, S. Egg White Synthesis and Photoluminescence of Platelike Clusters of CeO₂ Nanoparticles. *Cryst. Growth Des.* **2007**, *7*, 950–955. [[CrossRef](#)]
53. Hailstone, R.K.; DiFrancesco, A.G.; Leong, J.G.; Allston, T.D.; Reed, K.J. A Study of Lattice Expansion in CeO₂ Nanoparticles by Transmission Electron Microscopy. *J. Phys. Chem. C* **2009**, *113*, 15155–15159. [[CrossRef](#)]
54. Zhang, F.; Chan, S.-W.; Spanier, J.E.; Apak, E.; Jin, Q.; Robinson, R.D.; Herman, I.P. Cerium oxide nanoparticles: Size-selective formation and structure analysis. *Appl. Phys. Lett.* **2002**, *80*, 127–129. [[CrossRef](#)]
55. Pan, C.; Zhang, D.; Shi, L.; Fang, J. Template-Free Synthesis, Controlled Conversion, and CO Oxidation Properties of CeO₂ Nanorods, Nanotubes, Nanowires, and Nanocubes. *Eur. J. Inorg. Chem.* **2008**, *2008*, 2429–2436. [[CrossRef](#)]
56. Papavasiliou, J.; Rawski, M.; Vakros, J.; Avgouropoulos, G. Avgouropoulos, A Novel Post-Synthesis Modification of CuO–CeO₂ Catalysts: Effect on Their Activity for Selective CO Oxidation. *ChemCatChem* **2018**, *10*, 2096–2106. [[CrossRef](#)]
57. Aboukais, A.; Skaf, M.; Hany, S.; Cousin, R.; Aouad, S.; Labaki, M.; Abi-Aad, E. A comparative study of Cu, Ag and Au doped CeO₂ in the total oxidation of volatile organic compounds (VOCs). *Mater. Chem. Phys.* **2016**, *177*, 570–576. [[CrossRef](#)]
58. Guo, X.; Zhou, R. Identification of the nano/microstructure of CeO₂(rod) and the essential role of interfacial copper-ceria interaction in CuCe(rod) for selective oxidation of CO in H₂-rich streams. *J. Power Sources* **2017**, *361*, 39–53. [[CrossRef](#)]
59. Carabineiro, S.A.C.; Bogdanchikova, N.; Avalos-Borja, M.; Pestryakov, A.; Tavares, P.B.; Figueiredo, J.L. Gold supported on metal oxides for carbon monoxide oxidation. *Nano Res.* **2011**, *4*, 180–193. [[CrossRef](#)]
60. Si, R.; Raitano, J.; Yi, N.; Zhang, L.; Chan, S.-W.; Flytzani-Stephanopoulos, M. Structure sensitivity of the low-temperature water-gas shift reaction on Cu–CeO₂ catalysts. *Catal. Today* **2012**, *180*, 68–80. [[CrossRef](#)]
61. Rao, K.N.; Bharali, P.; Thrimurthulu, G.; Reddy, B.M. Supported copper–ceria catalysts for low temperature CO oxidation. *Catal. Commun.* **2010**, *11*, 863–866. [[CrossRef](#)]
62. Zheng, X.; Zhang, X.; Wang, X.; Wang, S.; Wu, S. Preparation and characterization of CuO/CeO₂ catalysts and their applications in low-temperature CO oxidation. *Appl. Catal. A Gen.* **2005**, *295*, 142–149. [[CrossRef](#)]
63. Avgouropoulos, G.; Ioannides, T.; Matralis, H. Influence of the preparation method on the performance of CuO–CeO₂ catalysts for the selective oxidation of CO. *Appl. Catal. B* **2005**, *56*, 87–93. [[CrossRef](#)]
64. Du, P.-P.; Wang, W.-W.; Jia, C.-J.; Song, Q.-S.; Huang, Y.-Y.; Si, R. Effect of strongly bound copper species in copper–ceria catalyst for preferential oxidation of carbon monoxide. *Appl. Catal. A Gen.* **2016**, *518*, 87–101. [[CrossRef](#)]
65. Ning, J.; Dong, C.; Li, M.; Zhou, Y.; Shen, W. Dispersion of copper oxide species on nanostructured ceria. *J. Chem. Phys.* **2020**, *152*, 094708. [[CrossRef](#)]

66. Zabilskiy, M.; Djinovic, P.; Erjavec, B.; Dražić, G.; Pintar, A. Small CuO clusters on CeO₂ nanospheres as active species for catalytic N₂O decomposition. *Appl. Catal. B Environ.* **2015**, *163*, 113–122. [[CrossRef](#)]
67. Sun, S.; Mao, D.; Yu, J. Enhanced CO oxidation activity of CuO/CeO₂ catalyst prepared by surfactant-assisted impregnation method. *J. Rare Earths* **2015**, *33*, 1268–1274. [[CrossRef](#)]
68. Wu, Z.; Li, M.; Howe, J.; Meyer, I.H.M.; Overbury, S.H. Probing Defect Sites on CeO₂ Nanocrystals with Well-Defined Surface Planes by Raman Spectroscopy and O₂ Adsorption. *Langmuir* **2010**, *26*, 16595–16606. [[CrossRef](#)]
69. Gamarra, D.; Belver, C.; Fernández-García, M.; Martínez-Arias, A. Selective CO Oxidation in Excess H₂ over Copper–Ceria Catalysts: Identification of Active Entities/Species. *J. Am. Chem. Soc.* **2007**, *129*, 12064–12065. [[CrossRef](#)]
70. Arango-Díaz, A.; Moretti, E.; Talon, A.; Storaro, L.; Lenarda, M.; Núñez, P.; Marrero-Jerez, J.; Jiménez-Jiménez, J.; Jiménez-López, A.; Rodríguez-Castellón, E. Preferential CO oxidation (CO-PROX) catalyzed by CuO supported on nanocrystalline CeO₂ prepared by a freeze-drying method. *Appl. Catal. A Gen.* **2014**, *477*, 54–63. [[CrossRef](#)]
71. Mock, S.A.; Zell, E.T.; Hossain, S.T.; Wang, R. Effect of Reduction Treatment on CO Oxidation with CeO₂ Nanorod-Supported CuO Catalysts. *ChemCatChem* **2018**, *10*, 311–620. [[CrossRef](#)]
72. Moretti, E.; Lenarda, M.; Storaro, L.; Talon, A.; Frattini, R.; Polizzi, S.; Rodríguez-Castellón, E.; Jiménez-López, A. Catalytic purification of hydrogen streams by PROX on Cu supported on an organized mesoporous ceria-modified alumina. *Appl. Catal. B Environ.* **2007**, *72*, 149–156. [[CrossRef](#)]
73. Jia, A.-P.; Jiang, S.-Y.; Lu, J.-Q.; Luo, M.-F. Study of Catalytic Activity at the CuO–CeO₂ Interface for CO Oxidation. *J. Phys. Chem. C* **2010**, *114*, 21605–21610. [[CrossRef](#)]
74. Yao, S.; Mudiyansele, K.; Xu, W.; Johnston-Peck, A.C.; Hanson, J.C.; Wu, T.; Stacchiola, D.; Rodriguez, J.A.; Zhao, H.; Beyer, K.A.; et al. Unraveling the Dynamic Nature of a CuO/CeO₂ Catalyst for CO Oxidation in Operando: A Combined Study of XANES (Fluorescence) and DRIFTS. *ACS Catal.* **2014**, *4*, 1650–1661. [[CrossRef](#)]
75. Sun, J.; Zhang, L.; Ge, C.; Tang, C.; Dong, L. Comparative study on the catalytic CO oxidation properties of CuO/CeO₂ catalysts prepared by solid state and wet impregnation. *Chin. J. Catal.* **2014**, *35*, 1347–1358. [[CrossRef](#)]
76. Gamarra, D.; Cámara, A.L.; Monte, M.; Rasmussen, S.B.; Chinchilla, L.E.; Hungría, A.B.; Munuera, G.; Györfy, N.; Schay, Z.; Corberán, V.C.; et al. Preferential oxidation of CO in excess H₂ over CuO/CeO₂ catalysts: Characterization and performance as a function of the exposed face present in the CeO₂ support. *Appl. Catal. B Environ.* **2013**, *130–131*, 224–238. [[CrossRef](#)]
77. Lin, J.; Huang, Y.; Li, L.; Wang, A.; Zhang, W.; Wang, X.; Zhang, T. Activation of an Ir-in-CeO₂ catalyst by pulses of CO: The role of oxygen vacancy and carbonates in CO oxidation. *Catal. Today* **2012**, *180*, 155–160. [[CrossRef](#)]
78. Avgouropoulos, G.; Ioannides, T.; Papadopoulou, C.; Batista, J.; Hocevar, S.; Matralis, H.K. A comparative study of Pt/ γ -Al₂O₃, Au/ α -Fe₂O₃ and CuO–CeO₂ catalysts for the selective oxidation of carbon monoxide in excess hydrogen. *Catal. Today* **2002**, *75*, 157–167. [[CrossRef](#)]